Chemical Science

ROYAL SOCIETY OF CHEMISTRY

EDGE ARTICLE

View Article Online
View Journal | View Issue

Cite this: *Chem. Sci.*, 2024, **15**, 19466

All publication charges for this article have been paid for by the Royal Society of Chemistry

Received 5th September 2024
Accepted 1st November 2024

DOI: 10.1039/d4sc05998k

rsc.li/chemical-science

Double coordination shell modulation of nitrogen-free atomic manganese sites for enhancing oxygen reduction performance†

Xue Bai,[a] Yin Wang,[c] Jingyi Han,[a] Siyu Chen,[a] Xiaodi Niu *[b] and Jingqi Guan *[a]

The rational design and fabrication of the active sites of single-atom catalysts (SACs) remains the main breakthrough for efficient electrocatalytic oxygen reduction reaction (ORR). Although metal–nitrogen–carbon (M–N–C) materials have been reported to exhibit good ORR performance, the M–N bond is prone to oxidation and subsequent destruction in Fenton-like reactions. Here, we report a nitrogen-free Mn-based SAC (Mn–S_1O_4G-600) anchored on a nitrogen-free graphene substrate, where manganese is bound to four oxygen atoms and one sulfur atom across two different coordination shells. In 0.1 M KOH, the Mn–S_1O_4G-600 demonstrates a half-wave potential of 0.86 V and a high kinetic current density of 10.3 mA cm^{-2} at 0.6 V. Due to the lack of nitrogen coordination, the Mn–S_1O_4G-600 has good anti-Fenton reaction properties. Notably, the Mn–S_1O_4G-600-based zinc–air battery displays an open circuit voltage of 1.46 V and outstanding cycle stability, which is superior to Pt/C. Theoretical calculations reveal that the introduction of the second S-coordination layer increases the charge density of the manganese center and decreases the energy barrier. This work identifies a novel active coordination configuration model for the ORR, paving the way for innovative design and synthesis of efficient SACs.

Introduction

With the growing global need to reduce environmental impact and improve energy efficiency, fuel cells and metal–air batteries exhibit immense promise as next-generation energy systems.[1–5] Therein, metal–air batteries have attracted significant attention for their high safety, ease of assembly, and theoretically high energy density characteristics.[6] However, the adoption of metal–air batteries still faces major challenges, especially the catalytic efficiency and lifetime of their air cathodes, which are directly related to the efficiency and stability of the ORR.[7–9] As the core step of battery operation, the efficiency of ORR is closely related to battery power density and durability.[10,11] Unfortunately, the poor two-electron-transfer pathway common in batteries not only reduces efficiency, but also triggers the formation of hydrogen peroxide, causing corrosion to the anode, and even causing safety hazards such as leakage and explosions.[12–14] Therefore, improving the four-electron transfer selectivity of ORR has become a key issue to be solved urgently.

At present, catalysts based on precious metal Pt perform well in the ORR, but high cost, weak stability and toxicity problems limit their wide application.[15,16] In contrast, SACs with unique isolated metal sites and low-cost advantages, have opened a new avenue to develop the property of transition metal electrocatalysis.[17–21] The catalytic activity of SACs is definitively determined by a complex electronic environment formed by the electronic effects between the central atom and the surrounding ligand atoms.[22,23] Nitrogen atoms, due to their similar radii with carbon atoms and appropriate electronegativity, are often employed as heteroatoms to anchor metal atoms, and the incorporation of heteroatom substitution strategies within M–N_4 model is utilized to enhance electrocatalytic performance.[24,25] However, the long-term stability of M–N–C (M = Fe, Co, Ni, Mn, and Cu) has become a bottleneck due to their high sensitivity of M–N bonds to OH radicals.[26] In contrast, the introduction of the ligand oxygen atoms can make isolated Fe atoms with strong Fenton effect exposed to H_2O_2 solution and stability more than 50 h.[27] The coordination of oxygen not only improves the resistance to Fenton effect, but also regulates the electronic structure of the central metal, and optimizes the catalytic process. Taking Ni–O_4 as an example, the d-band center of Ni–O_4 is closer to the Fermi level than the traditional nitrogen coordination model, which means that oxygen atoms can significantly enhance the interaction between metal atoms and carriers, thus accelerating the reaction kinetics.[28] In addition, for metal-free carbon-based materials, oxygen group elements (such as oxygen, sulfur, selenium, *etc.*) play a more

[a]*Institute of Physical Chemistry, College of Chemistry, Jilin University, 2519 Jiefang Road, Changchun 130021, P. R. China. E-mail: guanjq@jlu.edu.cn*

[b]*College of Food Science and Engineering, Jilin University, Changchun 130062, P. R. China. E-mail: niuxd@jlu.edu.cn*

[c]*Inner Mongolia Key Laboratory of Carbon Nanomaterials, Nano Innovation Institute (NII), College of Chemistry and Materials Science, Inner Mongolia Minzu University, Tongliao 028000, China*

† Electronic supplementary information (ESI) available. See DOI: https://doi.org/10.1039/d4sc05998k

significant role than nitrogen atoms in determining the selectivity of the four electron pathways in oxygen reduction, suggesting that they may be more suitable coordination atoms.[29,30] For Mn-based SACs, although Fenton reaction has little effect on their stability, their initial catalytic activity still needs to be further improved and replacing the Mn–N bond with the Mn–O bond is an important direction.

In view of the potential and challenges of Mn-based SACs, this study focuses on improving the ORR performance by regulating the coordination configuration and electronic structure of isolated manganese sites. The existing regulatory strategies mainly focus on regulating the first coordination shell at the central Mn site, introducing heteroatoms N and O to form different types of tetragonal structures.[31–33] This method mainly regulates the adsorption strength of reaction intermediates at the active site by adjusting the d-band center of Mn. However, the right strength is difficult to obtain due to the limitations of the adjustable position. Even if a second metal is introduced to form a bimetallic site, the deactivation of the metal due to aggregation or overflow during the reaction is inevitable.[34] Herein, we propose a strategy to introduce a second layer of coordination atoms, aiming to further optimize the intrinsic ORR activity of Mn beyond the limitations. The introduction of a second layer coordination atom can not only further increase the flexible variability of the electronic structure, but also increase the effective short-range interaction beyond the limitation of Mn's electron orbitals, further optimizing Mn's intrinsic ORR activity. Due to the difficulty of synthesis, it is still challenging to study the second shell coordination and mechanism of SACs.

In this work, we successfully decorated isolated Mn atoms into nitrogen-free graphene through oxygen and sulfur coordination for enhanced ORR property. X-ray absorption structure (XAS) proved that the coordination configuration of Mn is Mn–S_1O_4, where Mn is directly connected to four O atoms and one S atom with different bond lengths. The catalyst demonstrated a half-wave potential of 0.86 V, and maintains 85% catalytic activity at a voltage of 0.6 V for 25 h under alkaline conditions. In addition, the zinc–air batteries assembled with the catalyst showed high open-circuit voltage and durability. Theoretical calculations showed that Mn–SO_4G displays a significantly reduced reaction barrier of step (*OH → * + H_2O) due to the increased electron density at the Mn site.

Results and discussion

Structural characterization

The synthesis diagram of Mn–S_1O_4G-600 is shown in Fig. 1a. The uniformly mixed solution of manganese sulfate and graphene oxide was freeze-dried to obtain the precursor containing 0.7 wt% Mn. Subsequently, sulfur powder was added to the precursor, which was annealed in a nitrogen-protected atmosphere at 600 °C for 2 h, yielding the Mn–S_1O_4G-600. The presence of sulfur species in the carbon substrate provides Mn anchoring sites, which contribute to Mn stabilization and further modulate the electron structure. According to Brunauer–Emmett–Teller (BET) characterization, the specific

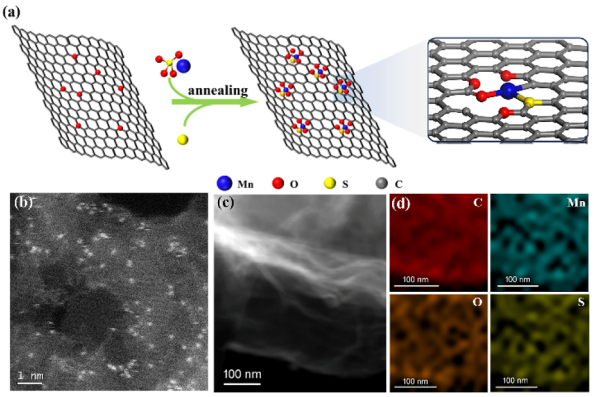

Fig. 1 (a) Synthetic illustration, (b) HAADF-STEM image, and (c and d) EDS elemental mappings of Mn–S_1O_4G-600.

surface area of Mn–S_1O_4G-600 was 556 m^2 g^{-1}, and no regular pore distribution was detected. In the high-angle annular dark-field scanning transmission electron microscope (HAADF-STEM) image, manganese atoms are shown as uniform-distributed bright spots due to higher reflected electron intensity than surrounding elements, demonstrating the feature of atomic-level dispersion (Fig. 1b). Fig. 1c and d shows the energy dispersive X-ray spectroscopy (EDS) elemental mapping images of Mn–S_1O_4G-600, which reveals uniform dispersion of Mn, O and S elements through the carbon substrate, indicating no significant agglomeration of Mn species. Further, in the XRD diagram, there is no peak of manganese-based nanoparticles, confirming the well distribution of isolated Mn single atoms (Fig. S1†).[35]

The electronic structure and coordination environment of the catalyst were determined by means of the K edge X-ray absorption spectroscopy (XAS). The edge absorption peak of Mn–S_1O_4G-600 is between manganese monoxide and manganese sesquioxide (Fig. 2a), indicating that the average valence of manganese is between 2 and 3. By further fitting the edge energy of the white line, the average valence of manganese in the Mn–S_1O_4G-600 is calculated to be 2.67 (Fig. 2b). Fig. 2c shows the Fourier transform of the extended X-ray absorption fine structure (EXAFS) spectrum. The absence of Mn–Mn contribution in the Mn–S_1O_4G-600 catalyst suggests that the Mn species are not in the form of metallic Mn nanoparticles or clusters,[36] confirming that monatomic Mn species were successfully constructed. The fitting results of EXAFS spectra reveal that the manganese in the Mn–S_1O_4G-600 is surrounded by five heteroatoms in two different shells (Fig. 2d). Specifically, the coordination number of Mn–O is 3.79 ± 0.23 and the distance is 1.970 ± 0.082 Å, which is slightly longer than that of symmetric Mn–$(N/O)_4$ plane structure (1.94 Å) (Table S1†).[37] The coordination number of Mn–S is 1.13 ± 0.15, and the distance is 2.14 ± 0.12 Å, shorter than that of Mn–N_2S_2 (2.34 Å) and Mn–N_3S_1 (2.5 Å) in conventional tetragonal configuration.[38,39] In addition, the wavelet transform (WT) contour map of Mn–S_1O_4G-600 displays only one maximum intensity at (1.5 Å, 4.7 $Å^{-1}$) (Fig. 2e and f), which is parallel with the maximum intensity of the first shell of Mn_2O_3 (1.5 Å, 7.5 $Å^{-1}$), indicating the bonding

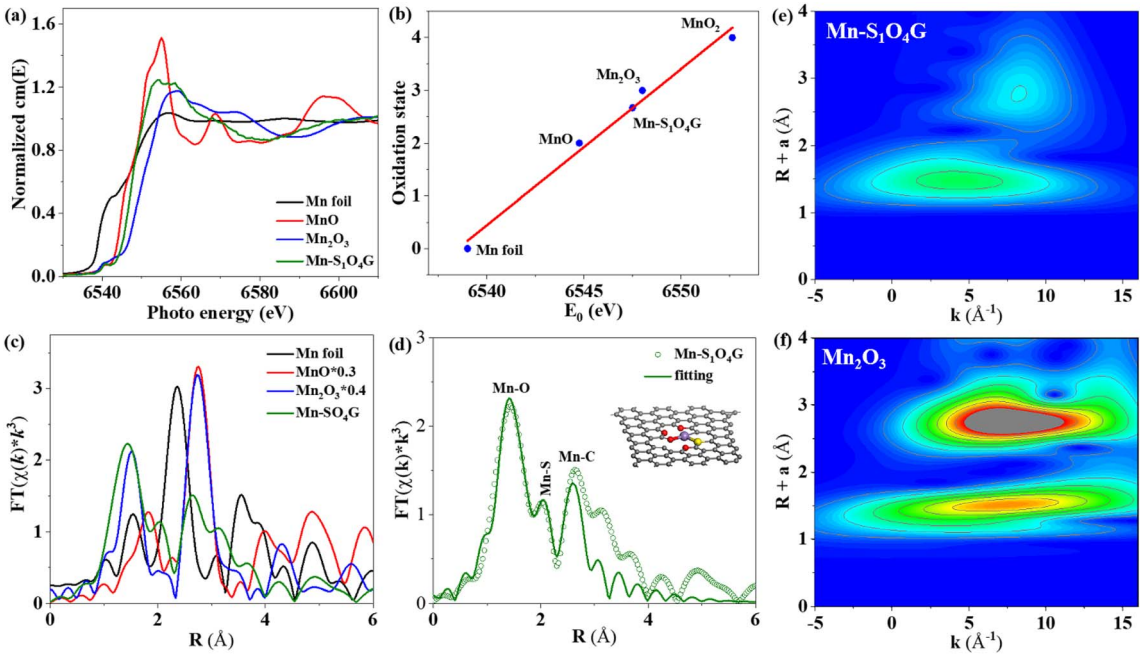

Fig. 2 (a) XANES spectra at Mn K-edge of the Mn–S_1O_4G-600, MnO, Mn_2O_3, and Mn foil. (b) Liner fitting for Mn valences derived from corresponding Mn K-edge XANES spectra. (c) FT-EXAFS spectra. (d) The fitting EXAFS spectrum for Mn–S_1O_4G (inset: the simulated structure). Wavelet transform (WT) of (e) Mn–S_1O_4G-600 and (f) Mn_2O_3 for the k^3-weighted EXAFS signals.

of Mn to O and non-bonding of Mn to Mn. Through the above analysis, Mn is anchored on the graphene by four oxygen atoms and one sulfur atom.

Electrocatalytic ORR performance

Electrocatalytic oxygen reduction performance tests were performed with a typical three-electrode system in oxygen-saturated 0.1 M KOH. According to CV curves of OG-600, SG-600, Mn–OG-600 and Mn–S_1O_4G-600 (Fig. S2†), all synthesized electrocatalysts show a clear cathodic reduction peak, and the Mn–S_1O_4G-600 catalyst shows the most positive oxygen reduction potential, suggesting the highest catalytic activity against ORR. From linear sweep voltammetry (LSV) curves (Fig. 3a), the catalyst Mn–S_1O_4G-600 shows high ORR activity, with an onset potential (E_0) of 0.98 V and a half-wave potential ($E_{1/2}$) of 0.86 V, outperforming OG-600, SG-600, Mn–OG-600 and Pt/C, whose $E_{1/2}$ are 0.73 V, 0.69 V, 0.78 V, and 0.84 V, respectively. Meanwhile, the Mn–S_1O_4G-600 displays higher kinetic current density (J_k = 10.3 mA cm^{-2}) than OG-600 (6.9 mA cm^{-2}), SG-600 (1.6 mA cm^{-2}), and Mn–OG-600 (5.0 mA cm^{-2}) at 0.6 V (Fig. 3b). Moreover, the Mn–S_1O_4G-600 has faster reaction kinetics due to smaller Tafel slope (46 mV dec^{-1}) than that of OG-600 (73 mV dec^{-1}), SG-600 (96 mV dec^{-1}) Mn–OG-600 (57 mV dec^{-1}), and Pt/C (79 mV dec^{-1}) (Fig. 3c). Hence, the Mn–S_1O_4G-600 exhibits remarkable ORR activity, surpassing commercial Pt/C and most other Mn-based catalysts reported previously (Table S2†). By measuring double-layer capacitance (C_{dl}), the electrochemical active surface areas (ECSA) of Mn–S_1O_4G-600 were counted as 217.5 cm^{-2}, larger than that of OG-600 (37 cm^{-2}), SG-600 (52 cm^{-2}), and Mn–OG-600 (177 cm^{-2}) (Fig. S3–S6†). Further, the fitting results of the equivalent circuit show that the catalyst Mn–S_1O_4G-600 exhibits the minimal impedance, indicative of rapid charge transfer (Fig. S7†).

To further understand the electron transfer process of ORR process on Mn–S_1O_4G-600, we recorded LSV curves at different rotational speeds on the RDE (Fig. 3d). The electron transfer number of ORR is calculated by Koutecky–Levich equation.[40] The catalysts show consistent linear relationship under different applied voltages. The electron transfer number of Mn–S_1O_4G-600 is about 4.0, which is close to that of Pt/C and Mn–OG-600 (Fig. S8 and S9†).[41] However, the ORR electron transfer number of OG-600 and SG-600 is only 1.9, indicating that the introduction of isolated Mn atom is the basis for the four-electron transfer of ORR (Fig. S10 and S11†). By collecting disk and ring current with RRDE, we further verify that the Mn–S_1O_4G-600 performs ORR mainly through four-electron transfer pathways, and the hydrogen peroxide efficiency is low (Fig. 3e and S12†).[42] After screening various calcination temperatures and the content of metal, we reveal that the optimal conditions involve doping both oxygen and sulfur at a calcination temperature of 600 °C, with a 0.7% Mn content (Fig. S13 and S14†).

To evaluate the ORR stability of the catalyst, CV cycling was performed in the voltage range 0.6–1.0 V. After 5000 CV cycles, the half-wave potential of Mn–S_1O_4G-600 is reduced by only 3 mV, which is better than 7 mV of Pt/C (Fig. 3f). In addition, the ORR current decay of the catalyst was investigated by chronoamperometry at a voltage of 0.6 V. As shown in Fig. S15,† the Mn–S_1O_4G-600 exhibits encouraging durability, maintaining 85% of its initial current density even after 25 hours of continuous operation, while Pt/C maintains only 47%. *In situ*

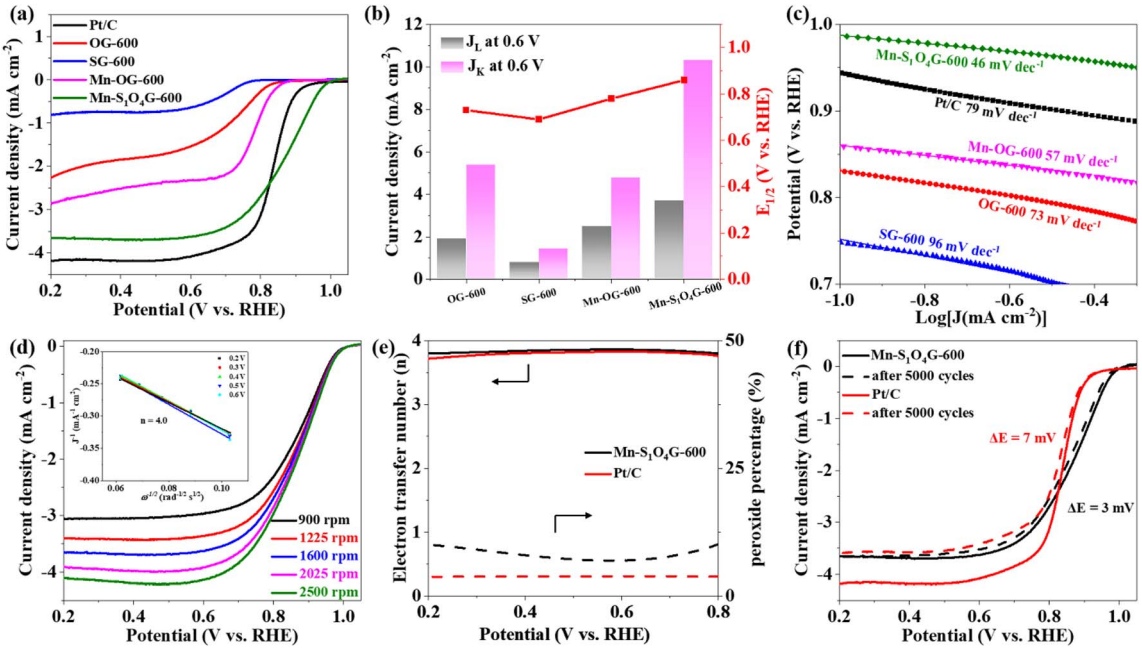

Fig. 3 ORR performance in oxygen-saturated 0.1 M KOH at room temperature. (a) LSV curves of Mn–S_1O_4G-600, Mn–OG-600, SG-600, OG-600, and Pt/C at 5 mV s^{-1} (the catalyst load was 0.47 mg cm^{-2} and the Pt/C load was 0.2 mg cm^{-2}). (b) Diffusion-limiting current density (J_L), kinetics current density (J_K) at 0.6 V and $E_{1/2}$. (c) Tafel slopes. (d) LSV curves of Mn–S_1O_4G-600 at the different rotating speeds from 900 rpm to 2500 rpm, and the inset is Koutecky–Levich plots and electron transfer number (*n*). (e) Electron transfer number and H_2O_2 yield of the Mn–S_1O_4G-600 and the Pt/C recorded by RRDE. (f) LSV curves of Mn–S_1O_4G-600 and Pt/C after 5000 CV cycles. The change in $E_{1/2}$ before and after 5000 CV cycles was represented by Δ*E*.

Raman spectroscopic analysis of Mn–S_1O_4G-600 at different potentials shows that the ratio of D and G bands in graphene does not change significantly, which represents that the catalyst maintains good structural stability during the reaction (Fig. S16†).

In addition, no peak is observed at 1150 cm^{-1} owing to the stretching of O–O, indicating that the catalyst can effectively prevent the adsorption of harmful peroxides and avoid the Fenton effect.[43] Significantly, XRD pattern of the catalyst operated at high voltage over a long period of time proves that there is no formation of manganese agglomeration (Fig. S17†). Furthermore, under the poisoning of 10 ppm KSCN, the half-wave potential of Mn–S_1O_4G-600 undergoes a notable decrease, attributable to the poisoning of Mn sites, illustrating Mn centers as the main active sites (Fig. S18a†). After methanol was added to the electrolyte, the ORR current density of Mn–S_1O_4G-600 decreased by only 5%, while that of Pt/C showed a sudden drop at 200 s, indicating a stronger tolerance of the Mn–S_1O_4G-600 to methanol (Fig. S18b†). In addition, when CO gas was introduced at 200 s, the catalyst showed a smaller current drop than Pt/C, and the performance showed a recovery trend when CO was stopped at 400 s, indicating that CO was less toxic to the active manganese site (Fig. S18c†).

Zinc–air battery (ZAB) performance

The oxygen evolution performance of the Mn–S_1O_4G-600 was tested in 0.1 M KOH, which reaches a current density of 10 mA cm^{-2} at an overpotential (η_{10}) of 360 mV (Fig. S19†). The small voltage difference (0.73 V) between η_{10} and $E_{1/2}$ shows the potential application of the catalyst in battery devices. To demonstrate the application of Mn–S_1O_4G-600 in ZABs, we assembled a ZAB with zinc foil as the anode, 6 M KOH + 0.2 M $Zn(Ac)_2$ as the electrolyte, and carbon paper coated with Mn–S_1O_4G-600 (loading 1 mg cm^{-2}) as the air cathode (Fig. 4a). The ZAB based on Mn–S_1O_4G-600 exhibits an open-circuit voltage of 1.46 V and an excellent maximum powder density of 199 mW cm^{-2} at 425 mA cm^{-2}, which significantly surpasses that of Pt/C-based ZAB (1.42 V and 113 mW cm^{-2} @ 178 mA cm^{-2}) (Fig. 4b). As depicted in Fig. 4c, upon subjecting the battery to a stepwise increase in discharge current density from 0 to 20 mA cm^{-2}, the discharge voltage maintains a relatively stable plateau, signifying that the Mn–S_1O_4G-600-based battery has stable output capability. Fig. 4d displays that the Mn–S_1O_4G-600-based ZAB exhibits a high specific capacity of 750 mA h g_{Zn}^{-1}, achieving 91.4% of the theoretical specific capacity (820 mA h g_{Zn}^{-1}), which is much higher than that of Pt/C-based ZAB (644 mA h g_{Zn}^{-1}). In addition, the Mn–S_1O_4G-600-based battery exhibits negligible augmentation in charge–discharge voltage difference over 140 h charge–discharge cycling at a constant current density of 5 mA cm^{-2}, whereas Pt/C-based battery underwent serious deterioration after 50 h, underscoring exceptional durability and rechargeability of Mn–S_1O_4G-600 within the battery device (Fig. 4e). The performance of ZAB based on Mn–S_1O_4G-600 is better than that of most reported catalysts, as shown in Table S3,† highlighting the potential application of Mn–S_1O_4G-600 in energy storage devices.

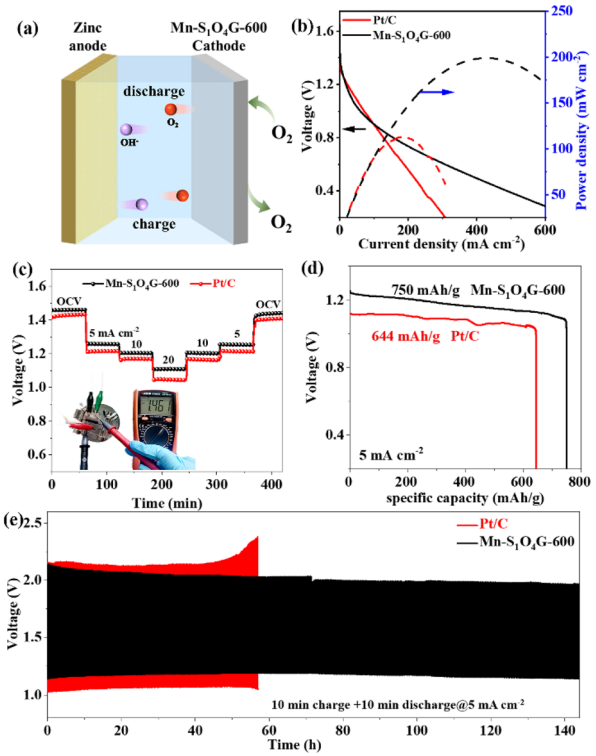

Fig. 4 (a) Schematic illustration of ZAB. (b) Discharging polarization and power density curves of Mn–S_1O_4G-600-based and Pt/C-based ZABs. (c) Galvanostatic discharge tests with various current densities for the Mn–S_1O_4G-600-based and Pt/C-based ZABs. (d) Specific discharging capacities at 5 mA cm^{-2}. (e) The charge/discharge cycling performance of Mn–S_1O_4G-600-based and Pt/C-based ZABs at 5 mA cm^{-2}.

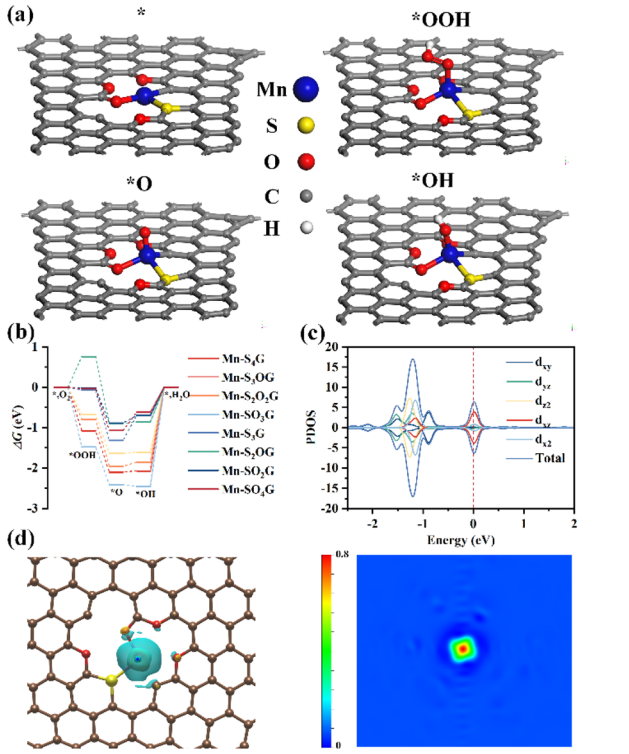

Fig. 5 (a) The proposed structures of the reaction intermediates at Mn–SO_4G site. (b) The free energy diagram for ORR of Mn–S_4G, Mn–S_3OG, Mn–S_2O_2G, Mn–SO_3G, Mn–S_3G, Mn–S_2OG, Mn–SO_2G, and Mn–SO_4G. (c) The projected DOS for Mn–SO_4G based on DFT calculations. (d) The charge density differences of Mn–SO_4G (yellow areas: the accumulation of charge density, and blue areas: depletion of charge density).

Study on ORR mechanism

To investigate the active sites and ORR mechanism, we conducted an in-depth exploration of the micro-reactive mechanism governing surface catalytic reactions on Mn–S_xO_yG, employing density functional theory (DFT) computational methods. To ensure the robustness of our model structures, we meticulously constructed eight distinct configurations: Mn–S_4G, Mn–S_3OG, Mn–S_2O_2G, Mn–SO_3G, Mn–S_3G, Mn–S_2OG, Mn–SO_2G, and Mn–SO_4G. Subsequently, we subjected our computational results to rigorous comparison with experimental data. As extensively documented in prior literature, the ORR pathway is characterized by the transformation of three key intermediate species: OH → O → OOH.[44] Therefore, we initiated our investigation by meticulously optimizing the geometries of these eight model structures and precisely determining the adsorption configurations of these intermediate species on the Mn–S_xO_yG catalytic surface, as vividly illustrated in Fig. 5a and S20–S26.†

Drawing upon the structural energies, we systematically construct the micro-reactive pathways for all eight model configurations, as elegantly depicted in Fig. 5b. The outcome of our meticulous analysis reveals a consistent trend among seven of the model structures, where the order of intermediate energies follows the sequence: *OOH > *O > *OH. Intriguingly, the Mn–S_2OG configuration stands apart from the rest. On the other hand, for the Mn–S_4G, Mn–S_3OG, Mn–S_2O_2G, and Mn–SO_3G models, a saliently high reaction barrier (ΔG > 1.00 eV) emerged in the *OH → * + H_2O reaction process, unmistakably designating this step as the rate-determining element in the micro-reactive sequence for these specific catalyst surfaces. In stark contrast, the Mn–S_3G, Mn–S_2OG, Mn–SO_2G, and Mn–SO_4G model structures exhibit significantly reduced reaction barriers during the *OH → * + H_2O reaction process. Notably, the Mn–SO_4G model surface showcases the lowest reaction barrier (0.62 eV) among all the studied catalyst models, thus manifesting superior catalytic activity.

Based on the DFT calculations, we derived the projected density-of-states (DOS) for Mn–SO_4G model (Fig. 5c). The DOS results indicate that the conduction and valence bands of Mn–SO_4G are well-aligned, facilitating charge carrier transfer and enhancing the catalytic ORR process. Additionally, we examined the charge density of the Mn–SO_4G model. Fig. 5d illustrates that the electron density of Mn atom in the Mn–SO_4G obviously increases due to the double-shell-coordination doped structure (O_4S_1). In conclusion, the higher catalytic activity of Mn–SO_4G is attributed to the double-shell-coordination doping, which aligns with the experimental findings.

Conclusions

In summary, a Mn-SAC was fabricated by one-pot mothed and utilizing the calcination temperature and metal ratio to regulate and create atomically dispersed Mn–S_1O_4G sites on the graphene. The XAS results reveal that four oxygen atoms and one sulphur atom are coordinated to one Mn atom, where the sulphur atom is located far from the first coordination shell. Due to the high selectivity for the four-electron transfer path and resistance to the Fenton effect, the catalyst Mn–S_1O_4G-600 exhibits excellent stability for the ORR, and the assembled ZAB shows better performance than commercial Pt/C. Further, theoretical calculations illustrate the structure of Mn–S_1O_4G has the lowest reaction barrier due to the modified d-band centre and the increase of charge density, which aligns perfectly with the experimental results. The work will help open a new road to develop nitrogen-free metal–oxygen/sulphur coordination model catalysts for the ORR and zinc–air batteries.

Data availability

The data supporting this article have been included as part of the ESI.†

Author contributions

Xue Bai: investigation, data Curation, writing – original draft; Yin Wang: investigation; Jingyi Han: investigation; Siyu Chen: investigation; Xiaodi Niu: investigation; Jingqi Guan: conceptualization, methodology, writing – review and editing, supervision.

Conflicts of interest

There are no conflicts to declare.

Acknowledgements

This work was supported by the National Natural Science Foundation of China (No. 22075099), and the Natural Science Foundation of Jilin Province (No. 20220101051JC). The authors thank BL11B beamline of the Shanghai Synchrotron Radiation Facility (SSRF) for providing the XAFS beamtime.

References

1 C. Zhang, W. Lv, Y. Tao and Q.-H. Yang, Towards superior volumetric performance: design and preparation of novel carbon materials for energy storage, *Energy Environ. Sci.*, 2015, **8**, 1390–1403.
2 A. G. Olabi, Q. Abbas, A. Al Makky and M. A. Abdelkareem, Supercapacitors as next generation energy storage devices: properties and applications, *Energy*, 2022, **248**, 123617.
3 S. K. Pradhan and B. Chakraborty, Battery management strategies: an essential review for battery state of health monitoring techniques, *J. Energy Storage*, 2022, **51**, 104427.
4 Z. Zhu, T. Jiang, M. Ali, Y. Meng, Y. Jin, Y. Cui and W. Chen, Rechargeable Batteries for Grid Scale Energy Storage, *Chem. Rev.*, 2022, **122**, 16610–16751.
5 J. Zhang, Z. Xia and L. Dai, Carbon-based electrocatalysts for advanced energy conversion and storage, *Sci. Adv.*, 2015, **1**, e1500564.
6 W. Shao, R. Yan, M. Zhou, L. Ma, C. Roth, T. Ma, S. Cao, C. Cheng, B. Yin and S. Li, Carbon-Based Electrodes for Advanced Zinc-Air Batteries: Oxygen-Catalytic Site Regulation and Nanostructure Design, *Electrochem. Energy Rev.*, 2023, **6**, 11.
7 J.-N. Liu, C.-X. Zhao, J. Wang, D. Ren, B.-Q. Li and Q. Zhang, A brief history of zinc–air batteries: 140 years of epic adventures, *Energy Environ. Sci.*, 2022, **15**, 4542–4553.
8 W. Sun, F. Wang, B. Zhang, M. Zhang, V. Küpers, X. Ji, C. Theile, P. Bieker, K. Xu, C. Wang and M. Winter, A rechargeable zinc-air battery based on zinc peroxide chemistry, *Science*, 2021, **371**, 46–51.
9 S. Chen, T. Wang, L. Ma, B. Zhou, J. Wu, D. Zhu, Y. Y. Li, J. Fan and C. Zhi, Aqueous rechargeable zinc air batteries operated at −110 °C, *Chem*, 2023, **9**, 497–510.
10 S. Zaman, L. Huang, A. I. Douka, H. Yang, B. You and B. Y. Xia, Oxygen Reduction Electrocatalysts toward Practical Fuel Cells: Progress and Perspectives, *Angew. Chem., Int. Ed.*, 2021, **60**, 17832–17852.
11 F. Dong, M. Wu, Z. Chen, X. Liu, G. Zhang, J. Qiao and S. Sun, Atomically Dispersed Transition Metal-Nitrogen-Carbon Bifunctional Oxygen Electrocatalysts for Zinc-Air Batteries: Recent Advances and Future Perspectives, *Nano-Micro Lett.*, 2021, **14**, 36.
12 M. Song, W. Liu, J. Zhang, C. Zhang, X. Huang and D. Wang, Single-Atom Catalysts for H_2O_2 Electrosynthesis via Two-Electron Oxygen Reduction Reaction, *Adv. Funct. Mater.*, 2023, **33**, 2212087.
13 W. Peng, J. Liu, X. Liu, L. Wang, L. Yin, H. Tan, F. Hou and J. Liang, Facilitating two-electron oxygen reduction with pyrrolic nitrogen sites for electrochemical hydrogen peroxide production, *Nat. Commun.*, 2023, **14**, 4430.
14 S. Li, L. Shi, Y. Guo, J. Wang, D. Liu and S. Zhao, Selective oxygen reduction reaction: mechanism understanding, catalyst design and practical application, *Chem. Sci.*, 2024, **15**, 11188–11228.
15 J. Liu, M. Jiao, B. Mei, Y. Tong, Y. Li, M. Ruan, P. Song, G. Sun, L. Jiang, Y. Wang, Z. Jiang, L. Gu, Z. Zhou and W. Xu, Carbon-Supported Divacancy-Anchored Platinum Single-Atom Electrocatalysts with Superhigh Pt Utilization for the Oxygen Reduction Reaction, *Angew. Chem., Int. Ed.*, 2019, **58**, 1163–1167.
16 J. Zhang, Y. Yuan, L. Gao, G. Zeng, M. Li and H. Huang, Stabilizing Pt-Based Electrocatalysts for Oxygen Reduction Reaction: Fundamental Understanding and Design Strategies, *Adv. Mater.*, 2021, **33**, 2006494.
17 X. Wang, Z. Kang, D. Wang, Y. Zhao, X. Xiang, H. Shang and B. Zhang, Electronic structure regulation of the Fe-based single-atom catalysts for oxygen electrocatalysis, *Nano Energy*, 2024, **121**, 109268.

18 Y. Wang, Y. Qu, B. Qu, L. Bai, Y. Liu, Z.-D. Yang, W. Zhang, L. Jing and H. Fu, Construction of Six-Oxygen-Coordinated Single Ni Sites on g-C_3N_4 with Boron-Oxo Species for Photocatalytic Water-Activation-Induced CO_2 Reduction, *Adv. Mater.*, 2021, **33**, 2105482.
19 H. Xu, D. Cheng, D. Cao and X. C. Zeng, RETRACTED ARTICLE: a universal principle for a rational design of single-atom electrocatalysts, *Nat. Catal.*, 2018, **1**, 339–348.
20 L. Xiao, Z. Wang and J. Guan, Optimization strategies of high-entropy alloys for electrocatalytic applications, *Chem. Sci.*, 2023, **14**, 12850–12868.
21 J. Han, X. Bai, X. Xu, X. Bai, A. Husile, S. Zhang, L. Qi and J. Guan, Advances and challenges in the electrochemical reduction of carbon dioxide, *Chem. Sci.*, 2024, **15**, 7870–7907.
22 S. Zago, L. C. Scarpetta-Pizo, J. H. Zagal and S. Specchia, PGM-Free Biomass-Derived Electrocatalysts for Oxygen Reduction in Energy Conversion Devices: Promising Materials, *Electrochem. Energy Rev.*, 2024, **7**, 1.
23 J. Zhang and M. Yu, Single-atom catalysts for neutral zinc-air batteries, *Sci. China Mater.*, 2024, **67**, 1674–1675.
24 W. Zhang, J. Zhang, N. Wang, K. Zhu, C. Yang, Y. Ai, F. Wang, Y. Tian, Y. Ma, Y. Ma, X. Zhang, L. Duan, D. Chao, F. Wang, D. Zhao and W. Li, Two-electron redox chemistry via single-atom catalyst for reversible zinc–air batteries, *Nat Sustainability*, 2024, **7**, 463–473.
25 T. Tang, X. Bai, Z. Wang and J. Guan, Structural engineering of atomic catalysts for electrocatalysis, *Chem. Sci.*, 2024, **15**, 5082–5112.
26 S. Huang, Z. Qiao, P. Sun, K. Qiao, K. Pei, L. Yang, H. Xu, S. Wang, Y. Huang, Y. Yan and D. Cao, The strain induced synergistic catalysis of FeN_4 and MnN_3 dual-site catalysts for oxygen reduction in proton-/anion- exchange membrane fuel cells, *Appl. Catal., B*, 2022, **317**, 121770.
27 Y. Wu, Y. Ding, X. Han, B. Li, Y. Wang, S. Dong, Q. Li, S. Dou, J. Sun and J. Sun, Modulating coordination environment of Fe single atoms for high-efficiency all-pH-tolerated H_2O_2 electrochemical production, *Appl. Catal., B*, 2022, **315**, 121578.
28 Z.-H. Zhou, W.-H. Li, Z. Zhang, Q.-S. Huang, X.-C. Zhao and W. Cao, Ni–O_4 as Active Sites for Efficient Oxygen Evolution Reaction with Electronic Metal–Support Interactions, *ACS Appl. Mater. Interfaces*, 2022, **14**, 47542–47548.
29 S. Pal, S. Bawari, T. Veettil Vineesh, N. Shyaga and T. N. Narayanan, Selenium-Coupled Reduced Graphene Oxide as Single-Atom Site Catalyst for Direct Four-Electron Oxygen Reduction Reaction, *ACS Appl. Energy Mater.*, 2019, **2**, 3624–3632.
30 H. W. Kim, V. J. Bukas, H. Park, S. Park, K. M. Diederichsen, J. Lim, Y. H. Cho, J. Kim, W. Kim, T. H. Han, J. Voss, A. C. Luntz and B. D. McCloskey, Mechanisms of Two-Electron and Four-Electron Electrochemical Oxygen Reduction Reactions at Nitrogen-Doped Reduced Graphene Oxide, *ACS Catal.*, 2020, **10**, 852–863.
31 Y. Qin, C. Guo, Z. Ou, C. Xu, Q. Lan, R. Jin, Y. Liu, Y. Niu, Q. Xu, Y. Si and H. Li, Regulating single-atom Mn sites by precisely axial pyridinic-nitrogen coordination to stabilize the oxygen reduction, *J. Energy Chem.*, 2023, **80**, 542–552.
32 Z. Lin, H. Huang, L. Cheng, Y. Yang, R. Zhang and Q. Chen, Atomically Dispersed Mn within Carbon Frameworks as High-Performance Oxygen Reduction Electrocatalysts for Zinc–Air Battery, *ACS Sustain. Chem. Eng.*, 2020, **8**, 427–434.
33 Y. Yang, K. Mao, S. Gao, H. Huang, G. Xia, Z. Lin, P. Jiang, C. Wang, H. Wang and Q. Chen, O-, N-Atoms-Coordinated Mn Cofactors within a Graphene Framework as Bioinspired Oxygen Reduction Reaction Electrocatalysts, *Adv. Mater.*, 2018, **30**, 1801732.
34 X. Xu and J. Guan, Spin effect in dual-atom catalysts for electrocatalysis, *Chem. Sci.*, 2024, **15**, 14585–14607.
35 H. Shang, W. Sun, R. Sui, J. Pei, L. Zheng, J. Dong, Z. Jiang, D. Zhou, Z. Zhuang, W. Chen, J. Zhang, D. Wang and Y. Li, Engineering Isolated Mn–N_2C_2 Atomic Interface Sites for Efficient Bifunctional Oxygen Reduction and Evolution Reaction, *Nano Lett.*, 2020, **20**, 5443–5450.
36 Z. Guo, Y. Xie, J. Xiao, Z.-J. Zhao, Y. Wang, Z. Xu, Y. Zhang, L. Yin, H. Cao and J. Gong, Single-Atom Mn–N_4 Site-Catalyzed Peroxone Reaction for the Efficient Production of Hydroxyl Radicals in an Acidic Solution, *J. Am. Chem. Soc.*, 2019, **141**, 12005–12010.
37 X. Wang, D. Wu, S. Liu, J. Zhang, X.-Z. Fu and J.-L. Luo, Folic Acid Self-Assembly Enabling Manganese Single-Atom Electrocatalyst for Selective Nitrogen Reduction to Ammonia, *Nano-Micro Lett.*, 2021, **13**, 125.
38 X. Bai, J. Han, S. Chen, X. Niu and J. Guan, Improvement of oxygen evolution activity on isolated Mn sites by dual-heteroatom coordination, *Chin. J. Catal.*, 2023, **54**, 212–219.
39 X. Bai, L. Wang, B. Nan, T. Tang, X. Niu and J. Guan, Atomic manganese coordinated to nitrogen and sulfur for oxygen evolution, *Nano Res.*, 2022, **15**, 6019–6025.
40 S. E. Treimer, A. P.-C. Tang and D. C. J. E. Johnson, *A Consideration of the Application of Koutecký-Levich Plots in the Diagnoses of Charge-Transfer Mechanisms at Rotated Disk Electrodes*, 2002, vol. 14, pp. 165–171.
41 R. Zhou, Y. Zheng, M. Jaroniec and S.-Z. Qiao, Determination of the Electron Transfer Number for the Oxygen Reduction Reaction: From Theory to Experiment, *ACS Catal.*, 2016, **6**, 4720–4728.
42 L. Bouleau, S. Pérez-Rodríguez, J. Quílez-Bermejo, M. T. Izquierdo, F. Xu, V. Fierro and A. Celzard, Best practices for ORR performance evaluation of metal-free porous carbon electrocatalysts, *Carbon*, 2022, **189**, 349–361.
43 Y. Zhao, H.-C. Chen, X. Ma, J. Li, Q. Yuan, P. Zhang, M. Wang, J. Li, M. Li, S. Wang, H. Guo, R. Hu, K.-H. Tu, W. Zhu, X. Li, X. Yang and Y. Pan, Vacancy Defects Inductive Effect of Asymmetrically Coordinated Single-Atom Fe–N_3S_1 Active Sites for Robust Electrocatalytic Oxygen Reduction with High Turnover Frequency and Mass Activity, *Adv. Mater.*, 2024, **36**, 2308243.
44 J. Qin, H. Liu, P. Zou, R. Zhang, C. Wang and H. L. Xin, Altering Ligand Fields in Single-Atom Sites through Second-Shell Anion Modulation Boosts the Oxygen Reduction Reaction, *J. Am. Chem. Soc.*, 2022, **144**, 2197–2207.